Nonlinear Model Predictive Control of J_2-Perturbed Impulsive Transfer Trajectories in Long-Range Rendezvous Missions

Sanaz Samsam[a], Robin Chhabra[a,*]

[a]*Department of Mechanical and Aerospace Engineering, Carleton University, Ottawa, K1S 5B6, Ontario, Canada*

Abstract

This paper develops a Nonlinear Model Predictive Control (NMPC) strategy for robust tracking of multi-impulse smooth transfer trajectories in J_2-perturbed orbital environments. The reference trajectories are designed for long-range rendezvous of servicing satellites with orbiting targets. In the proposed NMPC, the control signals are velocity increments at the impulse times, and the prediction horizon is variable due to the impulsive nature of the reference trajectories. The reference control input and the impulse times are pre-specified by the reference trajectory. Then, the NMPC calculates the optimal correction control vector to track the trajectory with minimum deviation and control effort, during the time between two consecutive impulses. To arrive near the target at the end of the transfer, the optimization in the last horizon is modified to be free-final-time, with an added soft constraint to minimize the final distance between the servicer and the target satellite. To avoid singularities in the mean dynamics of the J_2-perturbed

*Corresponding Author
Email address: robin.chhabra@carleton.ca (Robin Chhabra)

servicer, the equinoctial orbital elements are used in the process model. We also include the first-order long-periodic effects in this model. We investigate the robustness of the proposed NMPC in a simulation environment that additionally models: (i) the first-order short-periodic effects, (ii) a bounded uncertain acceleration to capture unmodelled dynamics, and (iii) burning time for satellite thrusters. Finally, an evolutionary optimization algorithm is implemented and embedded in the controller to decrease the computational complexity and to handle impulsive control inputs. Simulation results are provided to illustrate the tracking effectiveness of the developed controller.
Keywords: On-orbit servicing, Long-range rendezvous, Multi-impulse maneuver, Nonlinear Model Predictive Control, Optimal Tracking Guidance, Genetic algorithm

1. Introduction

On-Orbit Servicing (OOS) missions have been playing a significant role in space exploration. These missions include a range of services to operative satellites (hereinafter called target), such as debris removal, refueling, repairing, and assembly, to increase their efficiency and lifetime [1]. Such services are often performed using a servicing satellite, called servicer. The phase of a servicing mission that mostly contributes to fuel and time consumption is the long-range rendezvous [2]. Hence, the guidance and control in the long-range rendezvous phase must be comprehensively studied as one of the crucial steps in improving the performance of OOS missions. Long-range rendezvous in two-body context has been widely studied in the literature [3, 4] (and the references therein). However, neglecting the effect of environmental pertur-

bations results in inaccurate transfer trajectories that must be corrected by using a control strategy.

Satellites in different orbital altitudes experience various disturbances due to other celestial objects, Earth's oblateness, Earth's atmosphere, solar radiation, etc. Among these, the most dominant one from the Low Earth Orbit (LEO) regime to the Geostationary Earth Orbit (GEO) regime, which is a highly populated region, is the Earth's oblateness and especially the second zonal term (J_2) with orders of magnitude larger effects [5, 6]. The osculating orbital elements refer to the time-varying orbital elements of a satellite in a J_2-perturbed environment that represent the true position and velocity of a satellite. These elements poorly behave over time as a basis for prediction, since their numerical integration is extremely slow. The effects of the J_2 perturbation in the evolution of orbital elements are often divided into three types of induced motion, namely secular drift, short periodic effect, and long periodic effect [7]. Danielson *et al.* develop a semi-analytic approach using the equinoctial orbital elements for satellite orbit prediction by analytically integrating the periodic motions and finding the set of equations governing the secular drift [8]. Gim *et al.* derive the state transition matrices between the mean and osculating elements in both classical and equinoctial orbital elements [9, 10], using the 1^{st} order approximations of the long- and short-periodic motions obtained in [11]. Interested readers are referred to [12] and the references therein for more details about the recent developments in the analysis of J_2-perturbed orbits.

Designing optimization-based controllers for spacecraft established upon, e.g., dynamic programming, model predictive control, optimal control the-

ory, etc., is becoming popular due to the high efficiency demand in space applications [13]. Also, their capability of being combined with other control schemes, e.g., adaptive methods [14] and disturbance observers [15], demonstrates their flexibility and functionality. Among the optimization-based control strategies, Model Predictive Control (MPC) methods are of more interest due to their capability to handle mission related constraints [13, 16, 17, 18, 19, 20]. The MPC is equally applicable to linear and nonlinear systems, respectively referred to as Linear MPC (LMPC), and Nonlinear MPC (NMPC). Despite being fast, the LMPC is not sufficient for trajectory control in the long-range rendezvous missions, since the traveled orbital distance in these missions is large and the linear models fail to accurately capture satellite dynamics [21]. The methods for solving the NMPC are mainly based on nonlinear programming. The drawbacks of these gradient-based methods are increasing the complexity and the probability of converging to a local optimum that can be tackled by implementing heuristic optimization algorithms [22]. The efficacy of combining MPC with evolutionary algorithms has been studied in different research areas [23, 24, 25]. Tian *et al.* study the problem of cooperative search using a team of unmanned aerial vehicles and present an approach which combines MPC theory with the Genetic Algorithm (GA) to solve this problem [24]. The efficiency of solving MPC problems using GA to control the attitude maneuver of a satellite is demonstrated in [26]. One of the popular guidance approaches for space vehicles is reference trajectory tracking. There are several recent studies which have shown the effectiveness of the MPC in developing a reference tracking guidance method in real-time [27, 28, 29]. Authors in [27] present an MPC scheme incorporating neural-

dynamic optimization to achieve trajectory tracking of nonholonomic mobile robots. Moreover, Chai *et al.* propose both LMPC and NMPC schemes to solve the reconnaissance trajectory tracking problem [28]. The performance of MPC in real-time applications is highly dependent on the accuracy of the prediction model. Due to difficulties in providing an accurate model of a system, there is a need to guarantee the robustness under high levels of modeling uncertainty. One of the applicable approaches that ensures a Robust MPC (RMPC) is to add a bounded uncertainty function to the dynamic model [30, 31, 32]. A challenge in NMPC is that their closed-loop stability is not guaranteed. However, as is proved in [33], the stability of NMPC is guaranteed in the case of existing a fixed-final-state constraint.

The problem addressed in this paper is designing a real-time NMPC for a constrained spacecraft trajectory tracking problem specifically proposed for a long-range rendezvous mission. The trajectory that is used as the reference in this paper is a multi-impulse smooth trajectory that we designed in the context of two-body problem for chasing an orbiting target [4]. The objective function of the proposed NMPC is a combination of control efforts and tracking errors related to the reference trajectory following and target chasing at the final time. The optimization problems in the horizons before the last are fixed-time problems without considering any terminal constraints. However, to rendezvous with the target in an acceptable range, we solve a free-final-time optimization problem in the final horizon with the terminal condition of zero-distance from the target. To enhance the real-time performance of the developed NMPC, we: (i) include a nonlinear process model consisting of the well-behaved differential equations for secular drift and the analytic solu-

tion of the 1^{st}-order long-periodic motion, as the most dominant disturbing effects in a long-range rendezvous; and (ii) embed a GA-based optimization technique in the proposed impulsive NMPC. The motion is represented in equinoctial orbital elements to avoid singularities in the dynamical equations on circular and/or equatorial orbits. To robustly follow the reference trajectory in J_2-perturbed environments, a closed-loop system is constructed by receiving position and velocity feedback from the servicer. Further, since the impulsive controller is not achievable practically, we model the burning time, which is the time where the thruster is on, in the process model. Finally, we study the efficacy of the proposed GA-based NMPC in a numerical example. To demonstrate the robustness of the controller in this example, we include short-periodic effects and a bounded random acceleration, in addition to the secular and long-periodic effects, in the dynamic simulation of the servicer.

The remaining sections of this paper are organized as follows. The mathematical model describing the J_2 perturbation dynamics of a satellite represented in equinoctial orbital elements is given in Section 2. Then, a summary of our previous paper in modelling a multi-impulse smooth trajectory to chase a target [4] is given in Section 3. The developed NMPC architecture is then presented in Section 4. Section 5 reports some simulation results in a case study. Finally, Section 6 includes some concluding remarks.

2. Motion of Satellites in J_2-Perturbed Orbits

In this section, we discuss the orbital motion of a satellite in exposure to the J_2 perturbation effects. First, the equinoctial orbital elements are introduced, using which the dynamical equations of the perturbed satellites

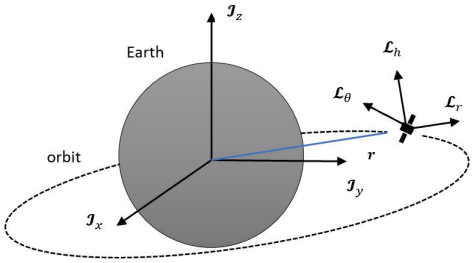

Figure 1: Local-vertical-local-horizontal and ECI reference frame

are never singular. The relationship between these elements, the classical orbital elements, and the Cartesian elements is discussed. Accordingly, the J_2-perturbed motion of satellites is approximated with mean elements and the first order of periodic effects.

2.1. Equinoctial Orbital Elements

There are different element sets for representing the orbital motion, e.g., the classical orbital elements (also known as Keplerian elements), equinoctial elements, Cartesian state vectors, Hill variables, cylindrical coordinates, and Deprit's ideal elements [34]. In this paper, we interchangeably use classical orbital elements, equinoctial elements, and Cartesian position and velocity vectors with respect to Earth-Centered Inertial (ECI) reference frame (this frame is denoted by $\Im$ in Fig. 1). Herein, we explain the conversions between these three sets of orbital elements. The Equinoctial Element (EE) set is denoted by the vector $\hat{\mathbf{x}} = [\hat{a} \quad \hat{h} \quad \hat{k} \quad \hat{p} \quad \hat{q} \quad \hat{\lambda}]^T$, which is constructed based on the classical orbital elements as follows [35]

$$\hat{a} = a, \quad \hat{h} = e\sin(\omega + \Omega), \quad \hat{k} = e\cos(\omega + \Omega), \tag{1}$$

$$\hat{p} = \tan(\iota/2)\sin(\Omega), \quad \hat{q} = \tan(\iota/2)\cos(\Omega),$$

$$\hat{\lambda} = \Omega + \omega + M. \tag{2}$$

Here, a is the semi-major axis, e is the eccentricity, ω is the argument of perigee, Ω is the Right Ascension of Ascending Node (RAAN), ι is the inclination angle, and M is the mean anomaly. Conversely, the classical orbital elements can be obtained from the EE by[8]:

$$a = \hat{a}, \quad e = \sqrt{\hat{h}^2 + \hat{k}^2}, \quad \iota = 2\arctan\sqrt{\hat{p}^2 + \hat{q}^2}, \tag{3}$$

$$\sin\Omega = \frac{\hat{p}}{\sqrt{\hat{p}^2 + \hat{q}^2}}, \quad \cos\Omega = \frac{\hat{q}}{\sqrt{\hat{p}^2 + \hat{q}^2}}, \quad \omega = \xi - \Omega,$$

$$M = \hat{\lambda} - \xi, \tag{4}$$

where ξ is defined by

$$\sin\xi = \frac{\hat{h}}{\sqrt{\hat{h}^2 + \hat{k}^2}}, \quad \cos\xi = \frac{\hat{k}}{\sqrt{\hat{h}^2 + \hat{k}^2}}. \tag{5}$$

The classical orbital elements then can be converted to the Cartesian coordinates whenever required [36]:

$$\mathbf{r} = \mathbf{Q}\mathbf{O}, \quad \dot{\mathbf{r}} = \mathbf{Q}\dot{\mathbf{O}},$$

$$\mathbf{O} = \frac{h^2}{\mu}\frac{1}{1 + e\cos\nu}[\cos\nu \quad \sin\nu \quad 0],$$

$$\dot{\mathbf{O}} = \frac{\mu}{h}[-\sin\nu \quad e + \cos\nu \quad 0], \tag{6}$$

$$\mathbf{Q} = \begin{pmatrix} \cos\omega\cos\Omega - \sin\omega\cos\iota\sin\Omega & -\sin\omega\cos\Omega - \cos\omega\cos\iota\sin\Omega & \sin\iota\sin\Omega \\ \cos\omega\sin\Omega + \sin\omega\cos\iota\cos\Omega & -\sin\omega\sin\Omega + \cos\omega\cos\iota\cos\Omega & -\sin\iota\cos\Omega \\ \sin\omega\sin\iota & \cos\omega\sin\iota & \cos\iota \end{pmatrix}, \tag{7}$$

where ν is the true anomaly and is a function of the mean anomaly M, μ is the gravitational constant of the Earth (≈ 398601.2 km^{3}s^{-2}), h is the orbital specific angular momentum $h = \sqrt{\mu a(1-e^2)}$, and $\mathbf{Q}$ in (7) is the transformation matrix from the orbital frame (z-axis perpendicular to orbital plane, x-axis pointing to periapsis of the orbit) to the ECI. We denote the set of position and velocity vectors in the Cartesian coordinates by the vector $\mathbf{X} = [\mathbf{r}^T \quad \dot{\mathbf{r}}^T]^T$.

2.2. Approximation of Osculating Orbital Motion in EE

It is beneficial to describe the motion of a spacecraft in terms of mean orbital elements as it best describes the secular growth by removing the periodic effects, so the long-term behaviour of the spacecraft motion is immediately evident [37]. One way of describing the satellite's mean motion is to use the classical orbital elements. Despite its being intuitive, the spacecraft dynamics represented by the classical orbital elements is singular for circular and/or equatorial orbits. The singularity can be avoided by using equinoctial elements that can be converted into Classical elements, as shown in (1) and (3). We denote the mean equinoctial orbital elements by the vector $\mathbf{x} = [a \quad h \quad k \quad p \quad q \quad \lambda]^T$. Note that to show the mean EE we simply drop the hat from the osculating EE. The dynamics of the mean orbital elements of a spacecraft without any control input can be formulated as [38]:

$$\dot{\mathbf{x}}_i = n\delta_{i6} + \sum_{j=1}^{6} (\mathbf{x}_i, \mathbf{x}_j) \frac{\partial \mathcal{R}}{\partial \mathbf{x}_j}, \tag{8}$$

where $\mathbf{x}_i$ is the i^{th} element of the vector $\mathbf{x}$ ($i = 1, \cdots, 6$), $n = \sqrt{\frac{\mu}{a^3}}$ is the Kepler (mean) mean motion, δ_{i6} is the Kronecker delta which is equal to one

only when $i = 6$ and is zero otherwise. Also, $(\mathbf{x}_i, \mathbf{x}_j)$ is called the Poisson matrix and its entries are called the Poisson brackets. The Poisson brackets of the mean element $\mathbf{x}$ are defined by

$$(\mathbf{x}_i, \mathbf{x}_j) \triangleq \frac{\partial \mathbf{x}_i}{\partial \mathbf{r}} \cdot \frac{\partial \mathbf{x}_j}{\partial \dot{\mathbf{r}}} - \frac{\partial \mathbf{x}_i}{\partial \dot{\mathbf{r}}} \cdot \frac{\partial \mathbf{x}_j}{\partial \mathbf{r}}. \tag{9}$$

It is evident that $(\mathbf{x}_i, \mathbf{x}_i) = 0$, $(\mathbf{x}_i, \mathbf{x}_j) = -(\mathbf{x}_j, \mathbf{x}_i)$. Moreover, $\mathcal{R}$ is the mean perturbing potential due to J_2 represented in mean EE and is derived by averaging the osculating perturbing potential (which is given in [8]):

$$\mathcal{R} = \frac{J(\gamma^2 - \frac{1}{3})}{a^3(1-h^2-k^2)^{\frac{3}{2}}}, \quad J = \frac{3\mu R_e^2 J_2}{4}, \quad \gamma = \frac{1-p^2-q^2}{1+p^2+q^2}. \tag{10}$$

Here, R_e is the equatorial radius of Earth ($\approx$ 6371 km), and J_2 is the second zonal harmonic coefficient ($\approx 1.0826 \times 10^{-3}$). Having the fifteen independent Poisson brackets for the mean EE [35] and $\frac{\partial \mathcal{R}}{\partial \mathbf{x}}$ based on (10) [8], (8) transforms to:

$$\dot{\mathbf{x}} = \begin{pmatrix} 0 \\ \frac{Jk[3\gamma^2-1+2\gamma(p\alpha-q\beta)]}{\eta_1\eta_2^4 a^3} \\ -\frac{Jh[3\gamma^2-1+2\gamma(p\alpha-q\beta)]}{\eta_1\eta_2^4 a^3} \\ -\frac{\eta_3 J\beta\gamma}{\eta_1\eta_2^4 a^3} \\ -\frac{\eta_3 J\alpha\gamma}{\eta_1\eta_2^4 a^3} \\ \frac{J[(1+\eta_2)(3\gamma^2-1)+2\gamma(p\alpha-q\beta)]}{\eta_1\eta_2^4 a^3} + n \end{pmatrix}. \tag{11}$$

Here,

$$\begin{aligned} \eta_1 =& \sqrt{\mu a}, \quad \eta_2 = \sqrt{1-h^2-k^2}, \quad \eta_3 = 1+p^2+q^2, \\ \alpha =& -\frac{2p}{1+p^2+q^2}, \quad \beta = \frac{2q}{1+p^2+q^2}. \end{aligned} \tag{12}$$

To have a more precise dynamics for the motion of a satellite, the first order of long- and short-periodic effects can be added to the mean motion. The osculating equinoctial variables can be approximated as a function of the mean variables as follows [9]:

$$\hat{\mathbf{x}} \approx \mathbf{x} - J_2 R_e^2 (\mathbf{x}^{(lp)} + \mathbf{x}^{(sp)}), \tag{13}$$

where $\mathbf{x}^{(lp)}$ and $\mathbf{x}^{(sp)}$ denote the first order long and short period variations due to J_2 and are obtained from the generating functions as discussed in [9, 11]. The time evolution of $\mathbf{x}^{(lp)}$ and $\mathbf{x}^{(sp)}$ based on the mean EE is presented in Appendix A.

3. Multi-impulse Smooth Trajectories for Chasing Orbiting Targets

In this section, we aim to formulate a class of reference trajectories that are used as the desired trajectory in the control design, in Section 4. We review the class of planar smooth multi-impulse trajectories for chasing orbiting targets in the long-range rendezvous phase of on-orbit servicing missions [4]. The trajectories are designed using classical orbital elements in the context of the two-body problem. In [4], we also implemented a multi-objective constrained optimization to find the Pareto optimal trajectories amongst this class of trajectories based on both control effort and transfer time.

In a given plane identified by known ι and Ω, in the three-dimensional space, considering a central gravitational field, the satellite's motion is fully described by four orbital elements, i.e., a, e, ω, and ν. Using the polar coordinates of the plane (r, θ), depicted in Fig. 2, ν can be replaced by $\theta = \nu - \omega$

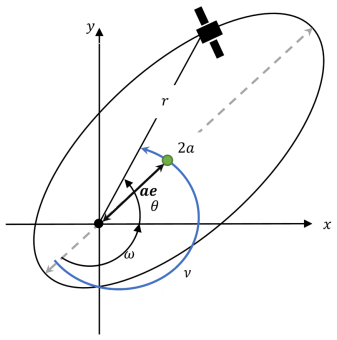

Figure 2: Oblique ellipse parameters in polar coordinates of a plane

to introduce the vector $\mathbf{p} = [a, e, \theta, \omega]^T$ as the set of planar orbital elements. The parameters r, ν, θ, a, e, and ω are shown in Fig. 2, where the origin is the Earth's center. In this framework, the reference trajectory for long-range rendezvous of a servicer can be developed by solving two problems of smoothness and chasing. In (Shakouri), it is shown that the constraints to generate N-impulse smooth trajectories between any two co-planar orbits are:

$$f_{i1}(\mathbf{p}_i, \mathbf{p}_{i+1}) := e_i \sin(\theta_i + \omega_i) + e_i e_{i+1} \sin(\omega_i - \omega_{i+1}) - e_{i+1} \sin(\theta_i + \omega_{i+1}) = 0, \tag{14}$$

$$f_{i2}(\mathbf{p}_i, \mathbf{p}_{i+1}) := a_i(1 - e_i^2)[1 + e_{i+1} \cos(\theta_i + \omega_{i+1})] - a_{i+1}(1 - e_{i+1}^2)[1 + e_i \cos(\theta_i + \omega_i)] = 0. \tag{15}$$

Here, the vectors $\mathbf{p}_i = [a_i, e_i, \theta_i, \omega_i]^T$, $i = 1, \cdots, N+1$, are the set of planar orbital elements describing the full satellite trajectory starting from $\mathbf{p}_1$ and ending at $\mathbf{p}_{N+1}$. Further, θ_i, for $i = 1, \cdots, N+1$, identifies the location of the i^{th} impulse. In the chasing problem, the co-planar orbital locations

of a servicer and a target are given at the time $t = 0$, and the aim is to find N-impulse smooth transfer trajectories for the servicer to intercept the target at its point of entry to the target's orbit. This problem can be solved using [4]:

$$f_3(\mathbf{p}_1, \cdots, \mathbf{p}_{N+1}) := (M_T(0) - M_N^+) + \sum_{i=1}^{N} (\frac{a_i}{a_T})^{\frac{3}{2}} (M_i^- - M_{i-1}^+) = 0. \tag{16}$$

Here, a_T and M_T denotes the semi-major axis and mean anomaly of the target. Also, M_i^+ and M_i^- are the mean anomalies of the sevicer at the i^{th} impulse in the $(i+1)^{st}$ and i^{th} orbit, respectively, which can be computed as a function of the vectors $\mathbf{p}_i$ and $\mathbf{p}_{i+1}$ [36]. Note that M_0^+ is equal to the servicer's initial mean anomaly in its parking orbit. The set of equations in (14)-(16) are highly nonlinear and can be solved using numerical algorithms, such as Newton method [4]. Once we have a solution, the magnitude of the velocity change at the i^{th} impulse location $\Delta v_i = \|\Delta \mathbf{v}_i\|$ is calculated based on the orbital elements of the smooth transfer trajectory by

$$\Delta v_i = v_i^+ - v_i^-, \tag{17}$$

where, $v_i^+ = \sqrt{\mu(\frac{2}{r_i} - \frac{1}{a_{i+1}})}$, $v_i^- = \sqrt{\mu(\frac{2}{r_i} - \frac{1}{a_i})}$, and

$$r_i = \frac{a_i(1 - e_i^2)}{1 + e_i \cos(\theta_i + \omega_i)}. \tag{18}$$

The velocity magnitude before and after the i^{th} impulse are denoted by v_i^- and v_i^+, respectively. The radius r_i is the radial component of the location of the servicer at the i^{th} impulse in polar coordinates, based on (18). Note that

at the i^{th} impulse location, the direction of $\Delta\mathbf{v}_i$ is the same as the servicer's velocity direction due to the smoothness conditions.

In addition, for an N-impulse trajectory, the transfer time t_f depends on the intermediate orbital elements, and is calculated by

$$t_f(\mathbf{p}_1, \cdots, \mathbf{p}_N) = \sum_{i=1}^{N} \Delta t_i(\mathbf{p}_i, \theta_{i-1}), \tag{19}$$

$$\Delta t_i(\mathbf{p}_i, \theta_{i-1}) = \frac{M_i^- - M_{i-1}^+}{\sqrt{\frac{\mu}{a_i^3}}}, \quad i = 1, \cdots, N. \tag{20}$$

Beside the constraints on the shape of the transfer trajectories and the two boundary conditions presented in (14)-(16), restrictions on the maximum permitted velocity increment and the orbital elements corresponding to the intermediate orbits can also be included in [4]. The latter restriction reduces the risk of collision in populated orbital regions and ensures that the servicer remains within the LEO regime. Note that in formulating the problem in (14)-(16) we did not consider any types of perturbations. In the next section, we design a controller to compensate the error of neglecting the J_2 perturbations.

4. Nonlinear Model Predictive Control

In the previous section, the trajectories were designed in the context of the two-body problem without involving any disturbances. In this section, we consider the following control problem to compensate for the errors of neglecting the most dominant J_2 perturbations in an orbit transfer.

Problem 4.1 (Tracking multi-impulse chasing trajectories)**.** Given a desired multi-impulse smooth trajectory for chasing a target, derived from (14)-(16),

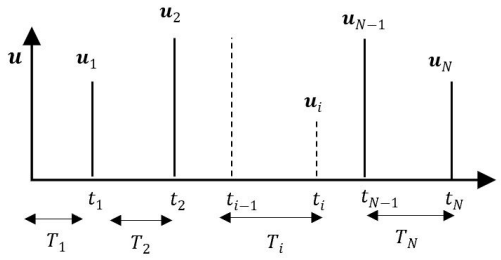

Figure 3: Impulsive control signals

find Δv_i at every impulse time t_i such that the satellite's trajectory under J_2 perturbations remains close to the desired trajectory and the satellite arrives near the target at the end of transfer.

To address this problem, a Nonlinear Model Predictive Control (NMPC) is proposed in this section. In most of the predictive control families, the idea is to calculate a control sequence minimizing an objective function using a model to predict the process output at future time instants (horizon) and applying the first control signal at each step (receding strategy) [39]. In the following, we introduce the nonlinear process model for the multi-impulse trajectory tracking problem and the objective function that should be minimized in the proposed NMPC. We also provide an optimization platform based on the GA to compute control signals, and its applicability to real-time problems is discussed in Section 5. The variable horizon that is considered in this control problem is the time difference between every two impulses denoted by $T_i, i = 1, \cdots, N$ (Fig. 3).

4.1. Nonlinear Process Model

Consider the following discrete-input nonlinear system governing the evolution of the mean EE for perturbed satellites:

$$\dot{\mathbf{x}}(t) = \mathbf{A}(\mathbf{x}(t)) + \sum_{i=1}^{N} \frac{\partial \epsilon(\hat{\mathbf{x}})}{\partial(\hat{\mathbf{x}})} \mathbf{B}(\hat{\mathbf{x}}(t)) \mathbf{u}_i \delta(t - t_i). \tag{21}$$

Here, $\mathbf{x} \in \mathbb{R}^6$ is the state space vector and includes mean equinoctial orbital elements, $\mathbf{A} : \mathbb{R}^6 \to \mathbb{R}^6$ is the nonlinear function of secular variation effects induced by J_2 perturbations given in (11), $\mathbf{u} \in \mathbb{R}^3$ is the control input in the spacecraft orbital frame, δ is the Dirac-delta function, t_i is the time of applying the i^{th} control impulse, and N is the maximum number of control impulses. Also, $\epsilon(\hat{\mathbf{x}})$ is a function that transforms osculating elements to mean elements ($\mathbf{x} = \epsilon(\hat{\mathbf{x}})$), and can be approximated by a 6×6 matrix whose diagonal elements are equal to 1 and the off-diagonal terms being of order J_2 or smaller [38]. Moreover, $\mathbf{B}$ in (22) is the 6×3 control influence matrix of Gauss's variational equations that relates accelerations in the spacecraft orbital frame to changes in the orbital elements [40]. In the control application, it is acceptable to approximate the term $\frac{\partial \epsilon(\hat{\mathbf{x}})}{\partial(\hat{\mathbf{x}})} \mathbf{B}(\hat{\mathbf{x}}(t))$ with $\mathbf{B}(\mathbf{x}(t))$ that is shown in (22).

$$\mathbf{B}(\mathbf{x}(t)) = \begin{pmatrix} \frac{2}{n\eta_2}(k\sin L - h\cos L) & \frac{2W}{n\eta_2} & 0 \\ -\frac{\eta_2 \cos L}{na} & \frac{\eta_2}{naW}[h + (1+W)\sin L] & -\frac{\eta_2 k}{naW}(p\cos L - q\sin L) \\ \frac{\eta_2 \sin L}{na} & \frac{\eta_2}{naW}[k + (1+W)\cos L] & \frac{\eta_2 h}{naW}(p\cos L - q\sin L) \\ 0 & 0 & \frac{\eta_2 \eta_3 \sin L}{2naW} \\ 0 & 0 & \frac{\eta_2 \eta_3 \cos L}{2naW} \\ -\frac{\eta_2}{naW}[\frac{W(h\sin L + k\cos L)}{1+\eta_2} + 2\eta_2] & -\frac{\eta_2}{naW}\frac{1+W}{1+\eta_2}(h\cos L - k\sin L) & -\frac{\eta_2}{naW}(p\cos L - q\sin L) \end{pmatrix}, \tag{22}$$

where

$$W = 1 + k\cos L + h\sin L, \quad L = \theta + \omega + \Omega. \tag{23}$$

The impulsive control signal $\mathbf{u}_i\delta(t-t_i)$(as shown in Fig. 3) is the velocity increment $\Delta\mathbf{v}_i$ over a small amount of time. As the impulsive control may cause severe damages to the satellite's equipment and it is not achievable practically, we assume that the thruster is on for a certain amount of time. This burn time Δt_{burn} is a function of satellite's initial mass m_0, thruster T, specific thrust I_{sp}, and an approximation of the magnitude of velocity increment Δv_{burn} [36].

$$\Delta t_{burn} = \frac{m_0 I_{sp} g_0}{T}(1 - e^{-\frac{\Delta v_{burn}}{I_{sp} g_0}}), \tag{24}$$

where $g_0 \approx 9.81\text{msec}^{-2}$ is the sea-level standard acceleration of gravity. Also, for a typical servicer satellite $T \approx 10\text{kN}$, $I_{sp} \approx 300\text{sec}$, and $\Delta v_{burn} \approx 1\text{kmsec}^{-1}$ [36]. Then, the velocity increment will be a constant amount over course of $\Delta t_{burn} \approx 30\text{sec}$, and is simply calculated as $\Delta\mathbf{v} = \Delta t_{burn}\mathbf{u}$.

The nonlinear process model that is considered for the evolution of the satellite in J_2 perturbed orbits includes the solution to (21) in addition to the first order long periodic effects, i.e., (A.1).

$$\hat{\mathbf{x}} \approx \mathbf{x} - J_2 R_e^2\, \mathbf{x}^{(lp)}, \tag{25}$$

where $\mathbf{x}^{(lp)} = [a^{(lp)}\, h^{(lp)}\, k^{(lp)}\, p^{(lp)}\, q^{(lp)}\, \lambda^{(lp)}]$. Since the NMPC feedback control law is most conveniently described in discrete time, a discrete-time formulation of the equations of motion is obtained. Considering a sampling time step T_s and a sampling instant j, by applying the Euler's approximation to the vehicle kinematics and dynamics, the discrete-time model can be formulated as shown in Appendix B.The equations in Appendix B can then be rewritten in a more compact form and the first-order long-periodic effect is

added to form the discrete-time nonlinear process model:

$$\begin{aligned}\mathbf{x}(j+1) &= f\big(\mathbf{x}(j), \mathbf{u}(j)\big) \in \mathbb{R}^6, \\ \hat{\mathbf{x}}(j+1) &= \mathbf{x}(j+1) - J_2 R_e^2\, \mathbf{x}^{(lp)}(j+1).\end{aligned} \tag{26}$$

4.2. Objective Function

To find the objective function, we need the following set of information provided by the desired multi-impulse trajectory (hereinafter called the reference trajectory): (i) the number of impulses N, (ii) the time of applying each impulse $(t_i, i = 1, \cdots, N)$, (iii) the prediction horizon $T_i, i = 1, \cdots, N$, (iv) the Δv from (17) and the resulted acceleration $\mathbf{u}_d = \frac{\Delta \mathbf{v}}{\Delta t_{burn}}$, and (v) the conversion of the reference trajectory to the Cartesian coordinates $(\mathbf{X}_d(t))$.

According to (26), the prediction of the dynamics conducted at the j^{th} time instant for τ time samples in the future is calculated as

$$\begin{aligned}\mathbf{x}(j+\tau+1|j) &= f\big(\mathbf{x}(j+\tau|j), \mathbf{u}(j+\tau|j)\big), \\ \hat{\mathbf{x}}(j+\tau+1|j) &= \mathbf{x}(j+\tau+1|j) - J_2 R_e^2\, \mathbf{x}^{(lp)}(j+\tau+1|j),\end{aligned} \tag{27}$$

where the notation $j+\tau|j$ indicates the predicted value of the variable at the instant $j+\tau$ calculated at time instant j.

The proposed objective function for the NMPC includes a norm of error between the desired and predicted satellite's trajectory under J_2 perturbation using the process model and a norm of control signals. To formulate the objective function, we use the Cartesian coordinates of the servicer and the target, due to the required numerical uniformity in the optimization problem. The equations that are needed to convert the EE to the classical orbital elements and then to the Cartesian coordinates are given in (1) and (6),

respectively. We denote the actual trajectory of the servicer at time t in a perturbed orbit, represented in the Cartesian coordinate, by $\hat{\mathbf{X}}(t)$. By introducing the error vector $\delta\mathbf{X} = \hat{\mathbf{X}} - \mathbf{X}_d$ and the correction vector $\delta\mathbf{u} = \mathbf{u} - \mathbf{u}_d$, the objective function for the NMPC to minimize the deviation from the desired trajectory with minimum control effort at the time t_i and in the prediction horizon T_{i+1} can be defined as

$$F_i(\delta\mathbf{X}, \delta\mathbf{u}) = \sum_{\tau=1}^{\bar{T}_{i+1}} \delta\mathbf{X}^T(\bar{t}_i + \tau|\bar{t}_i)\mathbf{Q}\delta\mathbf{X}(\bar{t}_i + \tau|\bar{t}_i) + \sum_{\tau=1}^{\bar{T}_{i+1}-1} \delta\mathbf{u}^T(\bar{t}_i + \tau|\bar{t}_i)\mathbf{R}\delta\mathbf{u}(\bar{t}_i + \tau|\bar{t}_i). \quad (28)$$

Here, we have $\bar{t}_i = \frac{t_i}{T_s}$, $\bar{T}_{i+1} = \frac{T_i}{T_s}$ for $i = 1, \cdots, N-2$. Note that $\delta\mathbf{X}(\bar{t}_i + \tau|\bar{t}_i)$ and $\delta\mathbf{u}(\bar{t}_i + \tau|\bar{t}_i)$ are the prediction of the error vector $\delta\mathbf{X}$ and the correction vector $\delta\mathbf{u}$ based on the nonlinear process dynamics (27) and converted into the Cartesian coordinate. Also, $\mathbf{Q} \in \mathbb{R}^{6\times6}$ and $\mathbf{R} \in \mathbb{R}^{3\times3}$ are symmetric positive definite matrices. The discrete time horizon over which F_i is minimized is $\tau = 1, ..., \bar{T}_{i+1}$. Note that the objective function F_i does not include the first interval T_1 and the time instants between impulses, since there is no control signal to compensate the deviation from the desired trajectory at the times other than t_i. That makes the objective function to be calculated $N-2$ times at the sampling instants $\bar{t}_i$. Therefore , to guarantee following the reference trajectory with minimum control effort in the time intervals T_{i+1} $(i = 1, \cdots, N-2)$, the following fixed-final-time constrained optimization is

solved at time t_i:

$$\delta\mathbf{u}^* = \arg\min_{\delta\mathbf{u}} \; F_i(\delta\mathbf{X}, \delta\mathbf{u}), \quad \text{for} \quad i = 1, \cdots, N-2$$

subject to: (i) (27) with the initial condition

$$\hat{\mathbf{X}}(\bar{t}_i|\bar{t}_i) = \hat{\mathbf{X}}(t_i),$$

and (ii) $\|\mathbf{u}(j+\tau+1|j)\| \leq u_{max}$, (29)

where u_{max} stands for the upper bound of the input vector. However, this optimization in T_N does not promise arriving at the target at the final time of transfer, which is the main goal in the long-range rendezvous mission, considered in this paper. Therefore, we add the (soft) constraint of zero distance between the servicer and the target at the final time to provide the chasing capability of the servicer. This constraint is augmented in the cost function with a large penalty constant absorbed into a weighting matrix. Moreover, since the resulting optimization problem may become over-constrained or difficult to solve while the final time is fixed, we consider the final time t_f or equivalently T_N among the design variables in the final horizon. Hence, the optimization problem in the final horizon becomes a free-final time constrained problem to ensure the chasing capability of the servicer. Denoting $\delta\mathbf{X}_T = \hat{\mathbf{X}} - \mathbf{X}_T$, where $\mathbf{X}_T$ is the target's state trajectory in the Cartesian coordinate, we define the objective function at the time t_{N-1} in the final

horizon T_N as

$$
\begin{aligned}
F_{N-1}(\delta\mathbf{X}, \delta\mathbf{u}) = & \\
& \sum_{\tau=1}^{\bar{T}_N} \delta\mathbf{X}^T(\bar{t}_{N-1}+\tau|\bar{t}_{N-1})\mathbf{Q}\delta\mathbf{X}(\bar{t}_{N-1}+\tau|\bar{t}_{N-1}) + \\
& \sum_{\tau=1}^{\bar{T}_N-1} \delta\mathbf{u}^T(\bar{t}_{N-1}+\tau|\bar{t}_{N-1})\mathbf{R}\delta\mathbf{u}(\bar{t}_{N-1}+\tau|\bar{t}_{N-1}) \\
& + \delta\mathbf{X}_T^T(\bar{t}_{N-1}+t_N|\bar{t}_{N-1})\mathbf{H}\delta\mathbf{X}_T(\bar{t}_{N-1}+t_N|\bar{t}_{N-1}), \qquad (30)
\end{aligned}
$$

where $\mathbf{H} \in \mathbb{R}^{6\times 6}$ is a symmetric positive definite matrix. Note that $\mathbf{Q}$, $\mathbf{H}$, and $\mathbf{R}$ are the weighting matrices to distinguish between the importance of following the desired path, penalizing the control, and catching the target satellite. The NMPC trajectory tracking algorithm minimizes the objective function subject to the dynamic constraints, path constraints, and terminal condition over the prediction horizon $\tau = 1, 2, ..., \bar{T}_N$. Then, the following free-final-time constrained optimization in the last horizon must be solved at the time t_{N-1}:

$$
\begin{aligned}
(\delta\mathbf{u}^*, t_N^*) &= \arg\min_{\delta\mathbf{u}, t_N} \; F_{N-1}(\delta\mathbf{X}, \delta\mathbf{u}), \\
\text{subject to: (i) (27) with the initial condition} & \\
& \hat{\mathbf{X}}(\bar{t}_{N-1}|\bar{t}_{N-1}) = \hat{\mathbf{X}}(t_{N-1}), \text{ and} \\
& \text{(ii) } \|\mathbf{u}(j+\tau+1|j)\| \le u_{max}. \qquad (31)
\end{aligned}
$$

The optimization problem given by (29) and (31) should be solved at t_i $(i = 1, \cdots, N-1)$, thereby calculating the optimal t_N and the constant optimal control signals over the course of Δt_{burn}. The last control signal $\mathbf{u}_N$ is reserved to match the servicer's and target's velocities at the time

of intersecting the target to complete the rendezvous mission. The overall NMPC algorithm and architecture are shown in Algorithm 1 and Fig. 4, respectively. As can be seen from Fig. 4, the state and control reference, i.e., $\mathbf{X}_d$ and $\mathbf{u}_d$, are obtained based on equations derived in the previous section. The closed-loop tracking guidance law is then achieved based on the designed NMPC. The NMPC optimization problem in (29) and (31) is solved using a genetic algorithm approach, which will be discussed in Section 4.3. The control input $\mathbf{u}(t)$ is then calculated by combining the reference control $\mathbf{u}_d$ and the correction control vector $\delta\mathbf{u}^*(t)$.

To investigate the performance of the proposed controller and show its robustness against unmodelled dynamics, in this paper we include a realistic dynamic simulation for the servicer in the control loop. In addition to secular and 1^{st} order long-periodic effects, the short-periodic effects and a bounded random uncertainty that is one order of magnitude smaller than the J_2 perturbations are simulated (see Fig. 4). To feedback the actual servicer states, the last calculated states of the servicer in the plant's dynamics in the current horizon is used as the initial states for the nonlinear process model of NMPC in (21) for the next horizon.

4.3. GA-based Optimization

The performance of the NMPC mainly depends on the implemented optimization algorithm. To solve the optimization problem defined in (29) and (31), we implement a single-objective GA. This GA method is a guided random search algorithm with the capability of exploring the diverse regions of the solution space. The employed GA method is explained in the flowchart depicted in Fig. 5. In the following, we elaborate the steps of the algorithm

Algorithm 1: Nonlinear Model Predictive Control.

Require: Servicer's initial location $\mathbf{x}_0$, Reference trajectory and control $\mathbf{X}_d$ and $\mathbf{u}_d$, target's trajectory $\mathbf{X}_T$, N, T_i, $i = 1, \cdots, N-1$, and sampling time T_s.

1. $t_N = \infty$, $j = 1$, $i = 2$.
2. $\mathbf{x}(j) = \mathbf{x}_0$.

while $j \leq \bar{t}_N$ **do**

if $j = \bar{t}_i$ **then**

if $i \neq N-1$ **then**

$\delta\mathbf{u}(j) \leftarrow \mathrm{GA}\Big(F\big(\delta\mathbf{X}(j), \delta\mathbf{u}_{candidate}(j)\big), T_i\Big)$ $\delta\mathbf{X}(j)$ is the feedback from the plant's dynamics to the control's dynamics.

3. $i \leftarrow i + 1$.

else

$[\delta\mathbf{u}(j), t_N] \leftarrow \mathrm{GA}\Big(F\big(\delta\mathbf{X}(j), \delta\mathbf{u}_{candidate}(j), t_{N_{candidate}}\big)\Big)$.

else

4. $\delta\mathbf{u}(j) \leftarrow 0$.
5. $\mathbf{u}(j) \leftarrow \delta\mathbf{u}(j) + \mathbf{u}_d(j) \pm \mathcal{O}(J_2/10)$.
6. $\mathbf{x}(j+1) \leftarrow \mathbf{x}(j) + T_s\Big(\mathbf{A}(\mathbf{x}(j)) + I_{6\times 6}\mathbf{B}(\mathbf{x}(j))\mathbf{u}^T(j)\Big)$.
7. $\hat{\mathbf{x}}(j+1) \leftarrow \mathbf{x}(j+1) - J_2 R_e^2\Big(\mathbf{x}^{lp}(j+1) + \mathbf{x}^{sp}(j+1)\Big)$. Calculating the plant's dynamics.
8. $\mathbf{x}(j)$ **is converted to** $\mathbf{X}(j)$.
9. $\delta\mathbf{X}(j) \leftarrow \mathbf{X}(j) - \mathbf{X}_d(j)$.
10. $j \leftarrow j + 1$.

return Real control signal $\mathbf{u}$, Real state space $\mathbf{X}$, and new transfer time t_N.

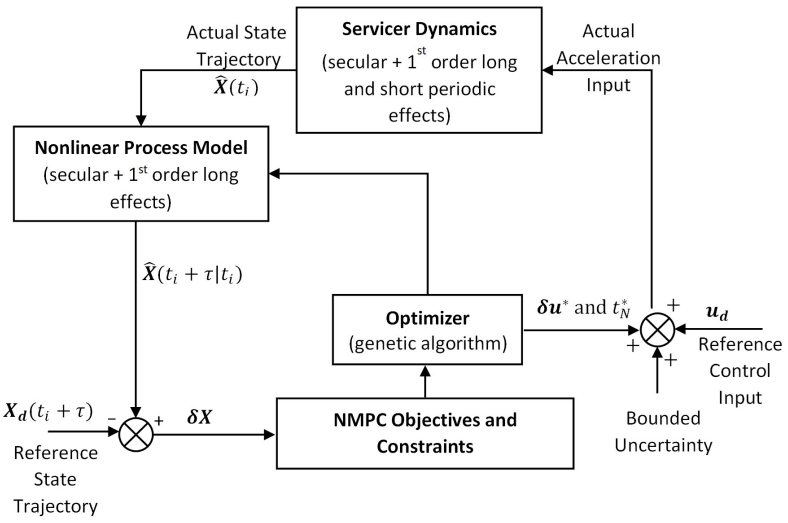

Figure 4: Block diagram of the closed-loop system

to find the optimal solutions in the proposed NMPC.

4.3.1. Initialization

The three design variables δu_x, δu_y and δu_z, which are the elements of the vector $\delta\mathbf{u}$ in the Cartesian coordinate, must be initialized for Z number of population at the time t_i, $i \neq N-1$. Population refers to a set (Z number) of design variables, which include the correction vector $\delta\mathbf{u}$ that is selected to be a small random vector in the initialization phase, and it is added to the desired control input $\mathbf{u}_d(t_i)$. For the last horizon, the time of catching the target specified T_N is another design variable beside $\delta\mathbf{u}$, to minimize the distance between the two satellites. For initializing this variable, we add a small random number to the transfer time we already have from the reference trajectory.

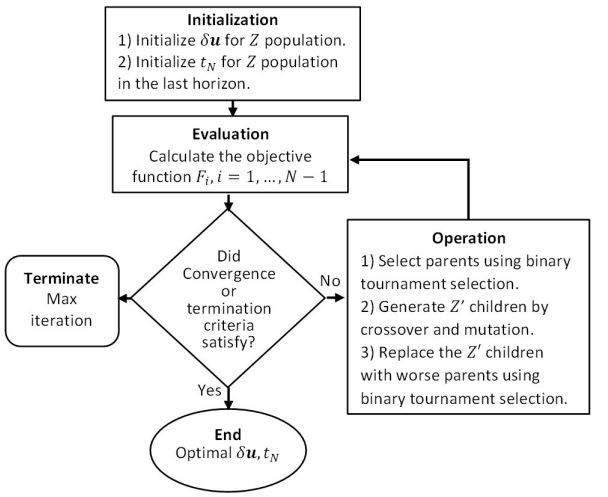

Figure 5: Single-objective genetic optimization architecture

4.3.2. Objective Function Evaluation

The next step is to evaluate the objective function for the initialized design variables. The objective function in the horizons $T_i, i \neq N$, is derived by (28), which measures the deviation of the servicer from the reference trajectory and the total control effort. Beside that, the objective function in the last interval also measures the distance of the servicer from the target at the final time t_f (which is among the initialized design variables). This performance criterion is prioritized through multiplying it by a large weighting matrix in (30).

4.3.3. Binary Tournament Selection

In any step of the optimization that we need to select parents, we use binary tournament selection method. In this method, two individuals are randomly chosen from the population and the one with the lower objective

function is kept in the process. To select other parents, we repeat the same procedure.

4.3.4. Arithmetic Crossover

Crossover is an inheritance operator, that causes the children to have attributes from all parents. Initially, a crossover rate (between 0 and 1) is fixed that is the indicator of the execution probability of this operator. During the optimization, each time that the crossover operator is called, a random number between 0 and 1 is generated. If this number is smaller than the crossover rate, then this operator is executed. During crossover, a random vector $\boldsymbol{\beta}$ (4-dimensional for the last horizon and 3-dimensional for other horizons) whose elements are between 0 and 1 is generated, based on which we define the children $\mathbf{y}_1^c, \mathbf{y}_2^c$ of the two selected parents by the binary tournament selection, $\mathbf{y}_1^p, \mathbf{y}_2^p$.

$$\begin{aligned} \mathbf{y}_1^c &= \boldsymbol{\beta} * \mathbf{y}_1^p + (\mathbf{1} - \boldsymbol{\beta}) * \mathbf{y}_2^p, \\ \mathbf{y}_2^c &= \boldsymbol{\beta} * \mathbf{y}_2^p + (\mathbf{1} - \boldsymbol{\beta}) * \mathbf{y}_1^p, \end{aligned} \tag{32}$$

where $\mathbf{y}$ is a vector of all design variables ($\delta\mathbf{u}$ and T_N), the operator $*$ refers to the element-wise multiplication of two vectors, and the vector $\mathbf{1}$ is the 3- or 4-dimensional vector whose elements are all equal to 1.

4.3.5. Mutation

In the iteration $1 \leq d \leq D$, where D is the maximum number of iterations, a number of individuals are randomly selected based on the binary tournament selection to be mutated with a probability, to explore the search region. A mutation probability distribution is fixed at the initialization phase

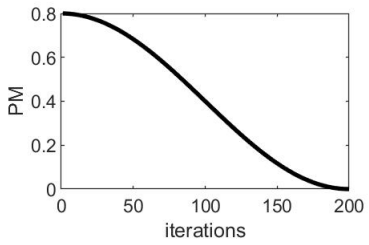

Figure 6: Mutation probability distribution

of the GA. This distribution allows the mutation operator to execute with a higher probability at the beginning of the optimization, which leads to avoiding convergence to local optima. In this paper, the mutation probability PM in the iteration d is defined by (see Fig. 6)

$$\mathrm{PM}(d) = \mathrm{PM}_0(1 + \cos\frac{\pi d}{D}),$$

where PM_0 is a parameter, fixed at the beginning of the optimization loop. Each time that the mutation operator is called for an individual, 3 random numbers (or 4 random numbers for the last horizon) between 0 and 1 are generated. If any of these numbers is smaller than $\mathrm{PM}(d)$, then the corresponding design variable in the individual is randomly reassigned within its bounds

4.3.6. Replacement

After applying the crossover and mutation operators on the current population, Z' children are generated and added to the current population. After evaluating the objective function of this new Z' individuals, they should be replaced with Z' number of the members of the old population to have a fixed number of individuals at each iteration. The replacement operation is

similar to the binary selection except that the higher objective function is chosen and replaced with the better offspring.

4.3.7. Termination Criteria and Convergence

In an optimization, several termination criteria can be considered: (i) maximum number of iterations, (ii) maximum number of iterations with no improvement, (iii) maximum allowed CPU time, and (iv) reaching an admissible fitness. Further, the convergence of a single objective heuristic algorithm is proved by a decreasing behaviour of the evaluated objective function over the course of iterations (for a minimization problem). In this paper, minimizing the objective function is numerically studied to ensure the convergence of the optimization in a case study. Further, the maximum number of iterations is considered as a termination criterion.

5. Numerical Example

In this section, we aim to evaluate the efficacy of the proposed nonlinear control strategy presented in Section 4 using a 5-impulse smooth reference trajectory ($N = 5$). In the following case study, the initial and final co-planar orbits are assumed to be in the plane specified by the inclination of $\iota = 5$ deg and RAAN of $\Omega = 10$ deg. These orbits are defined based on the planar orbital elements as:

$$a_S = 7000\,\text{km},\ e_S = 0.05,\ \omega_S = 10\,\text{deg},\ \theta_S(0) = 270\,\text{deg}$$

$$a_T = 7500\ \text{km},\ e_T = 0,\ \theta_T(0) = 0\,\text{deg}$$

Table 1 summarizes the co-planar 5-impulse smooth reference trajectory

Table 1: Information summary of the reference trajectory

Orbit number i	a [km]	e	ω [deg]	T_i [sec]	$\lvert\Delta\mathbf{v}_i\rvert$
1	7000	0.05	10	89.7	0.213
2	6640	0.06	-46.47	1885	0.255
3	6410	0.026	-37.41	2809	0.146
4	7930	0.174	108.13	1156	0.812
5	6390	0.173	-175.8	451.3	0.66
6	7500	0	60	-	-

considered in this study to catch the target from the servicer's parking orbit. The trajectory is described based on the (planar) classical orbital elements of the intermediate orbits, the time between each impulses T_i, and the magnitude of the velocity increment at the time of each impulse Δv_i. Fig. 7 depicts the reference trajectory in the plane of the orbits. The cyan star and the small red square show the initial locations of the servicer and target, and the black circles are the impulse locations. In the reference trajectory, the servicer catches the target at the final time $t_f = 6391$ sec.

In the NMPC, the weighting matrices appearing in F_i, for $i = 1, \cdots, 3$, corresponding to the trajectory error and control correction are designed to be $\mathbf{Q} = \mathbf{I}_{6\times 6}$ and $\mathbf{R} = 10\mathbf{I}_{3\times 3}$, respectively. For the last horizon, we design these matrices to be $\mathbf{Q} = 0.01\mathbf{I}_{6\times 6}$ and $\mathbf{R} = 0.1\mathbf{I}_{3\times 3}$, and the weighting matrix corresponding to the final distance from the target is selected to be $\mathbf{H} = 10\mathbf{I}_{6\times 6}$. Note that the weighting/penalty matrix $\mathbf{H}$ is designed orders of magnitude larger than the other two matrices to emphasise the importance of catching the target in the last interval. The time between each impulse T_i is the prediction horizon for the NMPC. The time of impulse (control

action) t_i, $i = 1, \cdots, 4$, can be obtained from T_i in Table 1, and for $i = 5$ the optimal time of the last impulse is calculated as part of the optimization of F_4. Moreover, the sampling time T_s, which is used to calculate the time instants $\bar{t}_i$, is set to be $T_s = 0.1$ sec.

The parameters of the genetic algorithm used in the NMPC architecture are designed as explained in the following. The typical value of the crossover rate used in the literature is $[0.8, 0.95]$ [41], and for constant mutation functions the rate is selected to be reciprocally proportional to the number of design variables, which is almost 0.3 in our case study. Hence, the crossover rate and PM_0 are chosen 0.8 and 0.3, respectively. Based on an investigation conducted on the optimization time and the quality of the produced solutions, the number of population and the maximum number of iterations are obtained to be $Z = 20$ and $D = 100$ for the GA before the last horizon, and $Z = 100$, $D = 200$ for the last horizon. Further, another termination criterion for the optimizations is to have a constant objective value (within a defined tolerance) for 50 consecutive iterations. Fig. 8 shows the obtained control signals in the Cartesian coordinates, after solving (29) and (31) using the GA. As one can observe, the control signal is a constant acceleration over the burning time $\Delta t_{burn} = 30\,\text{sec}$. In addition, in the last horizon we also find the optimal t_N to be 7266.4 sec, which indicates that the actual trajectory must be almost 14.6 min longer than the reference trajectory to catch the target. In Fig. 8, the control input at the final time t_N is obtained to match the velocity of the servicer with that of the target over Δt_{burn}.

The trajectory of the servicer is simulated under the secular and first order long-periodic and short-periodic effects induced by J_2, and bounded

random accelerations included to capture other types of perturbations with one order of magnitude smaller effects comparing to the J_2 perturbation. The reference trajectory along with the actual trajectory of the servicer in three-dimension are shown in Fig. 9, and their projections onto the x-y-plane are observed in Fig. 10.

The difference between the velocity increment vectors of the perturbed trajectory and the reference are shown in Fig. 11. The magnitudes of the velocity increment vectors at each impulse for the simulated trajectory are also shown in Table 2. Comparing the total velocity increment (control effort) for these two trajectories, the total velocity increment of the perturbed trajectory is slightly greater than that of the reference trajectory for 0.468 km/sec. This increment in the control effort is predictable since the controller has to compensate for the perturbing effects. As can be interpreted from Figs. 9-10, the servicer follows the trajectory before the 4^{th} impulse. However, in the last horizon after the 4^{th} impulse, servicer deviates from the reference. This is because of prioritizing catching the target to following the reference trajectory by giving more weight to the termination criterion in the last horizon. Due to the randomness of the added perturbation in the simulation, we computed the actual trajectory under the obtained optimal control input multiple times. The average distance between the two satellites at the final time of mission is calculated to be almost 4 km, with this distance changing in the range $[3, 5]$ km. Table 2 summarizes the averaged classical orbital elements in each intermediate orbit to compare with those corresponding to the reference trajectory. The classical orbital elements are averaged since they change over time due to the J_2 effects (especially the short-periodic

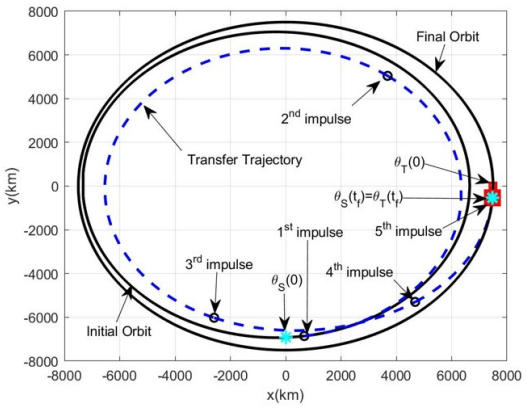

Figure 7: Reference multi-impulse smooth trajectory

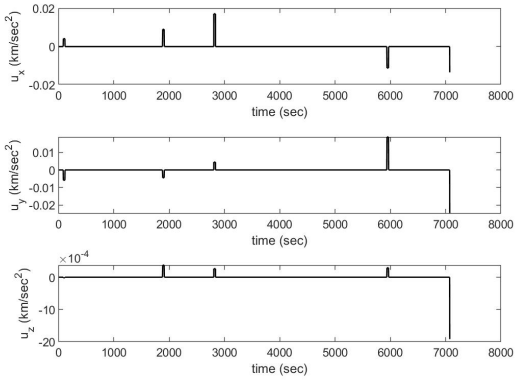

Figure 8: Control input generated by NMPC

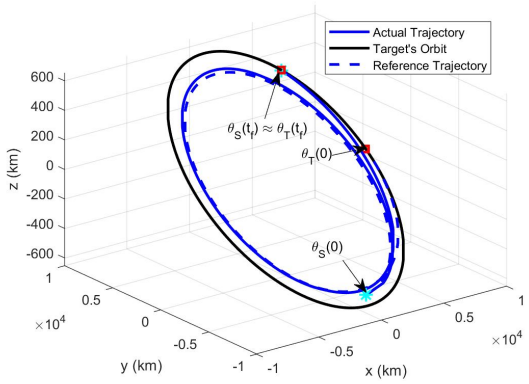

Figure 9: 3-D transfer trajectory

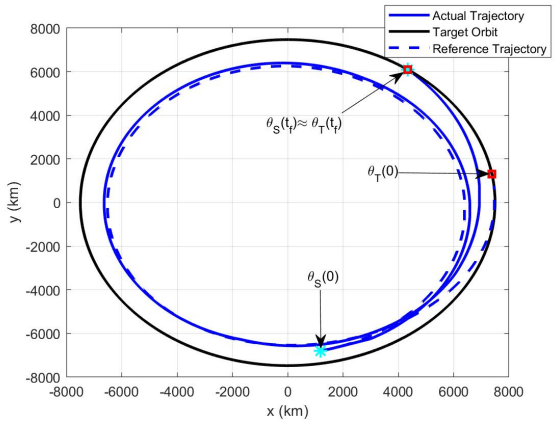

Figure 10: Projected 2-D transfer trajectory onto xy-plane

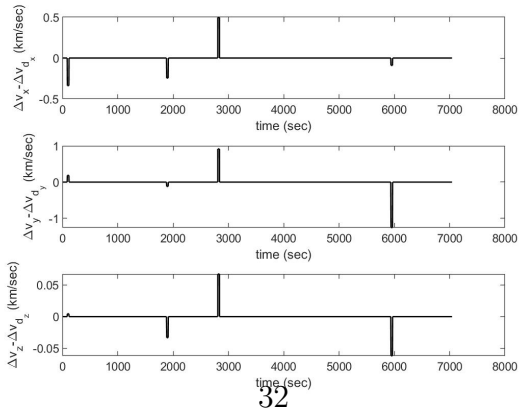

Figure 11: Velocity increment differences from the reference (ordered sequentially in x, y, z directions from top to bottom)

effect).

Table 2: Information summary of the simulated trajectory

Orbit number i	$\bar{a}$ [km]	$\bar{e}$	$\bar{\omega}$ [deg]	T_i [sec]	$\lvert\Delta\mathbf{v}_i\rvert$
1	7000	0.05	10	89.7	0.216
2	6680	0.051	67.03	1885	0.300
3	6450	0.029	-2.38	2809	0.530
4	6680	0.0451	186.93	1156	0.661
5	7820	0.121	-31.52	1326.6	0.852
6	7500	0	60	-	-

Although the stability of the NMPC is guaranteed when there is a terminal zero-state constraint [33], it is worth studying the performance of the optimizer at each prediction horizon. The convergence of single-objective evolutionary algorithms is shown using a decreasing behaviour of the objective function versus the number of objective function evaluations. In this regard, Figs. 12-15 show the convergence of the GA when optimizing F_i, $i = 1, \cdots, 4$. The distance from the target with respect to the number of objective function evaluations in the last interval is also given in Fig. 16. This figure indicates that the algorithm can converge to an acceptable distance from the target despite starting from an initial guess resulting in a very large distance. The GA method used in the NMPC scheme proposed in this paper is applicable in real time problems where the time between two impulses is longer than the corresponding optimization time. The average time to calculate the design variables ($\delta\mathbf{u}$ and T_N) before each impulse is around 6 minutes (on a PC with Core-i5 CPU and 12 GB of RAM) in the presented example, where the average time between two impulses is approximately 24 minutes. Note that by compromising the required accuracy, we can reduce the average optimization time to calculate the design variables.

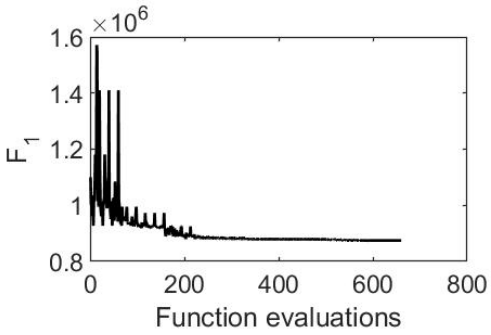

Figure 12: Convergence study for F_1

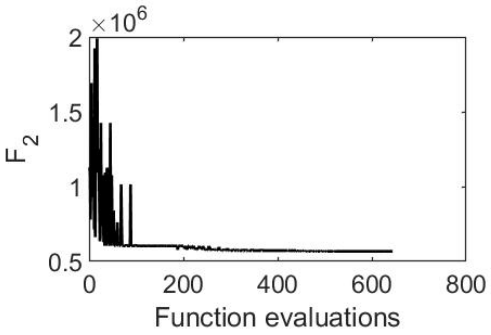

Figure 13: Convergence study for F_2

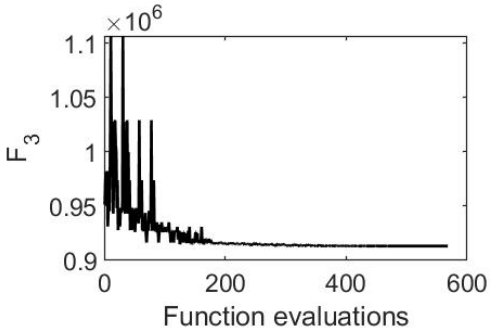

Figure 14: Convergence study for F_3

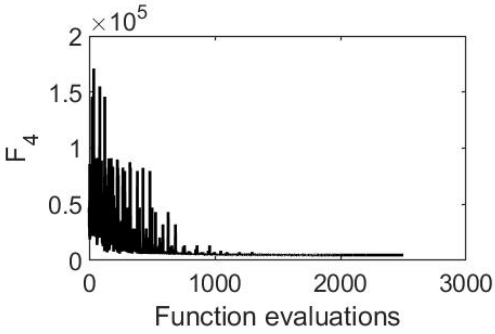

Figure 15: Convergence study for F_4

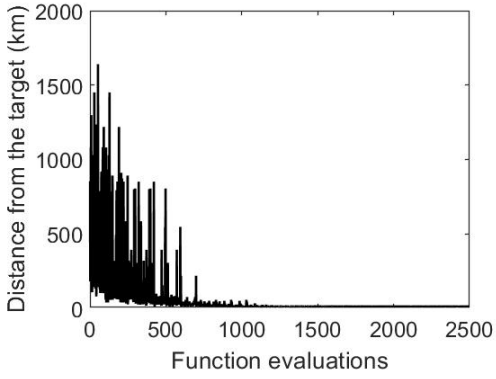

Figure 16: Distance from the target

6. Conclusion

In this paper, a robust NMPC model was developed and applied to solve the online optimal tracking in a long-range rendezvous problem in J_2 perturbed environments. The reference trajectory was a multi-impulse smooth transfer trajectory designed in the two-body context that we proposed in our previous work [4]. The control signals were non-zero constant accelerations over the burning time Δt_{burn}, since the impulsive control signal damages the satellites' structure.For the real-time servicer dynamics, secular, 1^{st} order long-periodic, and 1^{st} order short periodic effects induced by J_2 perturbation were considered. Further, to compensate for the error of neglecting other types of perturbations, a bounded random acceleration with one order of magnitude smaller effects comparing to the J_2 perturbation was added to the control signal. The optimization method applied in this paper was based on the GA that was designed to find the impulsive controllers and the final time in the final horizon. The objective functions of the unconstrained fixed-final-time optimization problems defined before the final horizon were the measure of deviation from the reference trajectory and the desired control input. To satisfy the chasing requirement, the optimization in the final horizon was a free-final-time problem with a terminal constraint.

The simulation results for a case, where the reference was a 5-impulse smooth trajectory, indicated that the proposed NMPC was able to follow the reference and catch the target with a final distance of about 4 km. This is an acceptable distance for the long-range rendezvous since the main goal of these missions is to just arrive at the target's orbit. Moreover, the transfer time and the control effort of the optimally controlled trajectory are slightly greater

(15 min and 0.468 km/sec, respectively) comparing to those of the reference trajectory. Finally, the convergence analysis shown in Figs. 12-16 indicated that the GA was well suited for the proposed NMPC. We have studied the proposed control scheme in at least 3 case studies to follow trajectories with 3 and 5 impulses. In these cases, the GA-based NMPC method was successful in performing impulsive trajectory following and arriving at a prespecified distance from the target satellite [42]. Therefore, it is effective to use the developed guidance algorithm for impulsive control signals to solve the online long-range rendezvous optimal trajectory tracking problems.

Acknowledgments

This work is supported by a grant from the Natural Sciences and Engineering Research Council of Canada (DGECR-2019-00085).

Appendix A. The First Order Long- and Short-Periodic Effects

$$a^{(lp)} = 0,$$

$$\lambda^{(lp)} = \left(\frac{\zeta_1 \zeta_2}{8a^2\eta^4(1+\eta)\sigma_2^2(\sigma_3^2 - \sigma_1^2)^2} \right) \left\{ 4\eta^2(\sigma_3^2 - \sigma_1^2)\Theta + (1+\eta)\Pi \right\},$$

$$
\begin{aligned}
L^{(lp)} &= \lambda^{(lp)} - \left(\frac{\Theta}{4a^2\eta^4(1+\eta)\sigma_2^2}\right) \\
&\qquad \times \left\{\zeta_1\zeta_2[3(1+\eta)+2\eta^2] + (1+\eta)[2(\tau_1\zeta_2+\tau_2\zeta_1)+\epsilon_1^2\tau_1\tau_2]\right\}, \\
h^{(lp)} &= -\left(\frac{1}{8a^2\eta^4\sigma_2^2(\sigma_3^2-\sigma_1^2)^2}\right) \times \left\{2\eta^2(q\zeta_2 - p\zeta_1)(\sigma_3^2-\sigma_1^2)^2\Theta + k\zeta_1\zeta_2\Pi\right\}, \\
k^{(lp)} &= -\left(\frac{1}{8a^2\eta^4\sigma_2^2(\sigma_3^2-\sigma_1^2)^2}\right) \times \left\{2\eta^2(q\zeta_1 + p\zeta_2)(\sigma_3^2-\sigma_1^2)^2\Theta + h\zeta_1\zeta_2\Pi\right\}, \\
p^{(lp)} &= -\left(\frac{\sigma_3}{16a^2\eta^4\sigma_2(\sigma_3^2-\sigma_1^2)^2}\right) \times \left\{5q\sigma_2^2\zeta_1\zeta_2 + (k\zeta_2 + h\zeta_1)(\sigma_3^2-\sigma_1^2)^2\Theta\right\}, \\
q^{(lp)} &= -\left(\frac{\sigma_3}{16a^2\eta^4\sigma_2(\sigma_3^2-\sigma_1^2)^2}\right) \times \left\{5p_2\sigma_2^2\zeta_1\zeta_2 - (k\zeta_1 - h\zeta_2)(\sigma_3^2-\sigma_1^2)^2\Theta\right\}.
\end{aligned}
\tag{A.1}
$$

$$
a^{(sp)} = -\left(\frac{(\sigma_3^2-2\sigma_1^2)}{a\eta^6\sigma_2^2}\right)\left[(1+\epsilon_2)^3 - \eta^3\right],
$$

$$
\begin{aligned}
\lambda^{(sp)} = &-\left(\frac{\epsilon_3(\sigma_3^2-2\sigma_1^2)}{2a^2\eta^4(1+\eta)\sigma_2^2(\sigma_3^2-\sigma_1^2)^2}\right)\left[(1+\epsilon_2)(2+\epsilon_2)+\eta^2\right] \\
&- \left(\frac{3(3\sigma_3^2-2\sigma_1^2)}{2a^2\eta^4\sigma_2^2}\right)[(L-\Lambda)+\epsilon_3],
\end{aligned}
$$

$$
L^{(sp)} = \lambda^{(sp)} + \left(\frac{\epsilon_3(\sigma_3^2-2\sigma_1^2)}{2a^2\eta^4(1+\eta)\sigma_2^2}\right)\left[(1+\epsilon_2)^2 + \eta(1+\eta)\right],
$$

$$
\begin{aligned}
h^{(sp)} = &-\left(\frac{h(\sigma_3^2-2\sigma_1^2)}{2a^2\eta^2(1+\eta)\sigma_2^2}\right) - \left(\frac{(\sigma_3^2-2\sigma_1^2)}{2a^2\eta^4\sigma_2^2}\right) \\
&\times \left\{h(1+\epsilon_2) + [\eta^2 + (1+\epsilon_2)(2+\epsilon_2)]\sin L\right\} \\
&- \left(\frac{3k(3\sigma_3^2-2)}{2a^2\eta^4\sigma_2^2}[(L-\lambda)+\epsilon_3]\right),
\end{aligned}
$$

$$
\begin{aligned}
k^{(sp)} = &- \left(\frac{k(\sigma_3^2 - 2\sigma_1^2)}{2a^2\eta^2(1+\eta)\sigma_2^2}\right) - \left(\frac{(\sigma_3^2 - 2\sigma_1^2)}{2a^2\eta^4\sigma_2^2}\right) \times \\
&\left\{k(1+\epsilon_2) + [\eta^2 + (1+\epsilon_2)(2+\epsilon_2)]\cos L\right\} \\
&+ \left(\frac{3h(3\sigma_3^2 - 2)}{2a^2\eta^4\sigma_2^2}[(L-\lambda) + \epsilon_3]\right),
\end{aligned}
$$

$$
p^{(sp)} = \left(\frac{3q\sigma_3}{2a^2\eta^4\sigma_2}\right)[(L-\lambda) + \epsilon_3],
$$

$$
q^{(sp)} = -\left(\frac{3p\sigma_3}{2a^2\eta^4\sigma_2}\right)[(L-\lambda) + \epsilon_3]. \tag{A.2}
$$

Here,

$$
\Theta = 1 + \frac{5\sigma_3^2}{2(\sigma_3^2 - \sigma_1^2)}
$$

$$
\Pi = 28 - 150\sigma_1^2 + 290\sigma_1^4 - 215\sigma_1^6 + 60\sigma_1^8 - 7\sigma_1^{10}
$$

$$
\begin{aligned}
&\eta = \sqrt{(1-h^2-k^2)}, \quad \epsilon_1 = \sqrt{k^2+h^2}, \\
&\epsilon_2 = k\cos L - h\sin L, \quad \epsilon_3 = k\sin L - h\cos L, \\
&\sigma_1 = \sqrt{q^2+p^2}, \quad \sigma_2 = 1+\sigma_1^2, \quad \sigma_3 = 1-\sigma_1^2, \\
&\tau_1 = q\cos L + p\sin L, \quad \tau_2 = q\sin L - p\cos L \\
&\zeta_1 = qk + ph, \quad \zeta_2 = qh - pk.
\end{aligned}
$$

Appendix B. Discrete-Time Equations for Mean Equinoctial Elements

$$
a(j+1) = a(j) + T_s\big(\frac{2}{n\eta_2}(k(j)\sin L(j) - h(j)\cos L(j))u_r + \frac{2W(j)}{n(j)\eta_2(j)}u_\theta\big),
$$

$$h(j+1) = h(j) + T_s\big(\frac{3\mu J_2 R_e^2 k(j)}{4\eta_2^4(j)\eta_1(j)a^3(j)}(3\gamma^2(j)-1+ 2\gamma(j)(p(j)\alpha(j)-q(j)\beta(j))) - \frac{\eta_2(j)\cos L(j)}{n(j)a(j)}u_r + \frac{\eta_2(j)}{n(j)a(j)W(j)}[h(j)+(1+W(j))\sin L(j)]u_\theta - \frac{\eta_2(j)k(j)}{n(j)a(j)W(j)}(p(j)\cos L(j)-q(j)\sin L(j))u_h\big),$$

$$k(j+1) = k(j) + T_s\big(-\frac{3\mu J_2 R_e^2 h(j)}{4\eta_2^4(j)\eta_1(j)a^3(j)}(3\gamma^2(j)-1+ 2\gamma(j)(p(j)\alpha(j)-q(j)\beta(j))) + \frac{\eta_2(j)\sin L(j)}{n(j)a(j)}u_r + \frac{\eta_2}{n(j)a(j)W(j)}[k(j)+(1+W(j))\cos L(j)]u_\theta + \frac{\eta_2 h}{n(j)a(j)W(j)}(p(j)\cos L(j)-q(j)\sin L(j))u_h\big),$$

$$p(j+1) = p(j) + T_s\big(-\frac{3\mu J_2 R_e^2 q(j)\eta_3(j)\beta(j)\gamma(j)}{4\eta_2^4(j)\eta_1(j)a^3(j)} + \frac{\eta_2(j)\eta_3(j)\sin L(j)}{2n(j)(j)a(j)W(j)}u_h\big),$$

$$q(j+1) = q(j) + T_s\big(-\frac{3\mu J_2 R_e^2 q(j)\eta_3(j)\alpha(j)\gamma(j)}{4\eta_2^4(j)\eta_1(j)a^3(j)} + \frac{\eta_2(j)\eta_3(j)\cos L(j)}{2n(j)a(j)W(j)}u_h\big),$$

$$\begin{aligned}\lambda(j+1) = \lambda(j) + T_s\big(&-\frac{3\mu J_2 R_e^2}{4\eta_2^4(j)\eta_1(j)a(j)^3}((3\gamma(j)^2-1)\\ &(\eta_2(j)+1) - 2\gamma(j)(p(j)\alpha(j)-q(j)\beta(j))) + n(j)\\ &-\frac{\eta_2(j)}{n(j)a(j)W(j)}\\ &[\frac{W(j)(h(j)\sin L(j)+k(j)\cos L(j))}{1+\eta_2(j)} + 2\eta_2(j)]u_r\\ &-\frac{\eta_2(j)}{n(j)a(j)W(j)}\frac{1+W(j)}{1+\eta_2(j)}(h(j)\cos L(j)\\ &-k(j)\sin L(j))u_\theta - \frac{\eta_2(j)}{n(j)a(j)W(j)}(p(j)\cos L(j)\\ &-q(j)\sin L(j))u_h\big).\end{aligned} \tag{B.1}$$

References

[1] Q. Hu, Y. Liu, Y. Zhang, Velocity-free saturated control for spacecraft proximity operations with guaranteed safety, IEEE Trans. Syst., Man, Cybern.,Syst (2021) 1–13doi:10.1109/TSMC.2021.3050507.

[2] P. Rousso, S. Samsam, R. Chhabra, A Mission Architecture for On Orbit Servicing Industrialization, in: IEEE Aerosp., 2021, pp. 1–14.

[3] A. Shirazi, J. Ceberio, J. A. Lozano, An evolutionary discretized lambert approach for optimal long-range rendezvous considering impulse limit, Aerosp. Sci. Technol. 94 (2019) 105400.

[4] S. Samsam, R. Chhabra, Multi-impulse smooth trajectory design for long-range rendezvous with an orbiting target using multi-objective non-dominated sorting genetic algorithm, Aerosp. Sci. Technol 120 (2022).

[5] C. Lücking, C. Colombo, C. R. McInnes, A passive satellite deorbiting strategy for medium earth orbit using solar radiation pressure and the j2 effect, Acta Astronaut. 77 (2012) 197–206.

[6] H. Schaub, K. T. Alfriend, J_2 invariant relative orbits for spacecraft formations, Celest. Mech. Dyn. Astron. 79 (2) (2001) 77–95.

[7] G. J. Der, R. Danchick, Conversion of osculating orbital elements to mean orbital elements, in: Flight Mechanics/Estimation Theory Symposium, 1996.

[8] D. A. Danielson, C. P. Sagovac, B. Neta, L. W. Early, Semianalytic satellite theory, Tech. rep., U.S. Naval Postgraduate School (1995).

[9] D.-W. Gim, K. T. Alfriend, Satellite relative motion using differential equinoctial elements, Celest. Mech. Dyn. Astron. 92 (4) (2005) 295–336.

[10] D.-W. Gim, K. T. Alfriend, State transition matrix of relative motion for the perturbed noncircular reference orbit, J. Guid. Control Dyn. 26 (6) (2003) 956–971. arXiv:https://doi.org/10.2514/2.6924, doi:10.2514/2.6924.
URL https://doi.org/10.2514/2.6924

[11] D. Brouwer, Solution of the problem of artificial satellite theory without drag, Astron. J. 64 (1274) (1959) 378–397.

[12] J. Wang, C. Liu, The j2 relative perturbation analysis of satellite formation under the requirement of relative position maintenance with millimeter-level accuracy, Int. J. Aerosp 2021 (2021).

[13] R. Chai, A. Tsourdos, A. Savvaris, S. Chai, Y. Xia, C. P. Chen, Review of advanced guidance and control algorithms for space/aerospace vehicles, Prog. Aerosp. Sci. 122 (2021) 100696.

[14] Z. Zhao, G. Cruz, D. S. Bernstein, Adaptive spacecraft attitude control using single-gimbal control moment gyroscopes without singularity avoidance, J. Guid. Control Dyn. 42 (11) (2019) 2342–2355.

[15] W.-H. Chen, J. Yang, L. Guo, S. Li, Disturbance-observer-based control and related methods—an overview, IEEE Trans. Ind. Electron. 63 (2) (2015) 1083–1095.

[16] X. Zhang, J. Ma, Z. Cheng, S. Huang, S. S. Ge, T. H. Lee, Trajectory generation by chance-constrained nonlinear mpc with prob-

abilistic prediction, IEEE Trans. Cybern. 51 (7) (2021) 3616–3629. doi:10.1109/TCYB.2020.3032711.

[17] Q. Wang, Z. Duan, Y. Lv, Q. Wang, G. Chen, Distributed model predictive control for linear–quadratic performance and consensus state optimization of multiagent systems, IEEE Trans. Cybern. 51 (6) (2021) 2905–2915. doi:10.1109/TCYB.2020.3001347.

[18] M. R. C. Qazani, H. Asadi, S. Nahavandi, A model predictive control-based motion cueing algorithm with consideration of joints' limitations for hexapod motion platform, in: 2019 IEEE Int. Conf. Syst. Man Cybern. SMC, 2019, pp. 708–713. doi:10.1109/SMC.2019.8914458.

[19] E. Camponogara, S. N. Talukdar, Distributed model predictive control: Synchronous and asynchronous computation, IEEE Trans. Syst., Man, Cybern.,Syst - Part A: Systems and Humans 37 (5) (2007) 732–745. doi:10.1109/TSMCA.2007.902632.

[20] M. Li, P. Zhou, H. Wang, T. Chai, Nonlinear multiobjective mpc-based optimal operation of a high consistency refining system in papermaking, IEEE Trans. Syst., Man, Cybern.,Syst 50 (3) (2020) 1208–1215. doi:10.1109/TSMC.2017.2748722.

[21] L. Ravikumar, R. Padhi, N. Philip, Trajectory optimization for rendezvous and docking using nonlinear model predictive control, IFAC-PapersOnLine 53 (1) (2020) 518–523.

[22] R. Chai, A. Savvaris, A. Tsourdos, Y. Xia, S. Chai, Solving multi-objective constrained trajectory optimization problem by an extended

evolutionary algorithm, IEEE Trans. Cybern. 50 (4) (2020) 1630–1643. doi:10.1109/TCYB.2018.2881190.

[23] S. Arrigoni, F. Braghin, F. Cheli, Mpc path-planner for autonomous driving solved by genetic algorithm technique, arXiv:2102.01211 (2021).

[24] J. Tian, Y. Zheng, H. Zhu, L. Shen, A mpc and genetic algorithm based approach for multiple uavs cooperative search, in: Int. Conf. Comput. Sci., Springer, 2005, pp. 399–404.

[25] A. Mohammadi, H. Asadi, S. Mohamed, K. Nelson, S. Nahavandi, Multiobjective and interactive genetic algorithms for weight tuning of a model predictive control-based motion cueing algorithm, IEEE Trans. Cybern. 49 (9) (2019) 3471–3481. doi:10.1109/TCYB.2018.2845661.

[26] M. TayyebTaher, S. M. Esmaeilzadeh, Model predictive control of attitude maneuver of a geostationary flexible satellite based on genetic algorithm, Adv. Space Res. 60 (1) (2017) 57–64.

[27] Z. Li, J. Deng, R. Lu, Y. Xu, J. Bai, C.-Y. Su, Trajectory-tracking control of mobile robot systems incorporating neural-dynamic optimized model predictive approach, IEEE Trans. Syst., Man, Cybern.,Syst 46 (6) (2016) 740–749. doi:10.1109/TSMC.2015.2465352.

[28] R. Chai, A. Savvaris, A. Tsourdos, S. Chai, Y. Xia, Optimal tracking guidance for aeroassisted spacecraft reconnaissance mission based on receding horizon control, IEEE Trans. Aerosp. Electron. Syst. 54 (4) (2018) 1575–1588.

[29] J. Shin, H. J. Kim, Nonlinear model predictive formation flight, IEEE Trans. Syst., Man, Cybern.,Syst - Part A: Systems and Humans 39 (5) (2009) 1116–1125. doi:10.1109/TSMCA.2009.2021935.

[30] U. Eren, A. Prach, B. B. Koçer, S. V. Raković, E. Kayacan, B. Açıkmeşe, Model predictive control in aerospace systems: Current state and opportunities, J. Guid. Control Dyn. 40 (7) (2017) 1541–1566.

[31] A. Mesbah, Stochastic model predictive control: An overview and perspectives for future research, IEEE Control Syst. 36 (6) (2016) 30–44. doi:10.1109/MCS.2016.2602087.

[32] J. Zhang, W. Zhao, G. Shen, Y. Xia, Disturbance observer-based adaptive finite-time attitude tracking control for rigid spacecraft, IEEE Trans. Syst., Man, Cybern.,Syst 51 (11) (2021) 6606–6613. doi:10.1109/TSMC.2019.2947320.

[33] G. De Nicolao, L. Magni, R. Scattolini, Stability and robustness of nonlinear receding horizon control, in: Nonlinear model predictive control, Springer, 2000, pp. 3–22.

[34] D. J. Gondelach, R. Armellin, Element sets for high-order poincaré mapping of perturbed keplerian motion, Celest. Mech. Dyn. Astron. 130 (10) (2018) 1–35.

[35] R. A. Broucke, P. J. Cefola, On the equinoctial orbit elements, Celest. Mech. Dyn. Astron. 5 (3) (1972) 303–310.

[36] H. D. Curtis, Orbital mechanics for engineering students, Elsevier, Butterworth-Heinemann, 2013.

[37] H. Schaub, K. T. Alfriend, Impulsive feedback control to establish specific mean orbit elements of spacecraft formations, J. Guid. Control Dyn. 24 (4) (2001) 739–745. arXiv:https://doi.org/10.2514/2.4774, doi:10.2514/2.4774.
URL https://doi.org/10.2514/2.4774

[38] H. Schaub, J. L. Junkins, Analytical Mechanics of Space Systems, 2nd Edition, AIAA Education Series, Reston, VA, 2009. doi:10.2514/4.867231.

[39] E. F. Camacho, C. B. Alba, Model predictive control, Springer science & business media, 2013.

[40] J. A. Kechichian, Trajectory optimization using nonsingular orbital elements and true longitude, J. Guid. Control Dyn. 20 (5) (1997) 1003–1009.

[41] K. Deb, A. Pratap, S. Agarwal, T. Meyarivan, A fast and elitist multiobjective genetic algorithm: Nsga-ii, IEEE Trans. Evol. Comput. 6 (2) (2002) 182–197.

[42] S. Samsam, an evolutionary framework for multi-objective trajectory design and robust model predictive control in long-range rendezvous missions, Master's thesis, Carleton University (2022).